A ''shunt'' Fabry–Perot resonator for high-frequency electron spin resonance utilizing a variable coupling scheme

Jeff P. Barnes and Jack H. Freed[a)]
Baker Laboratory of Chemistry, Cornell University, Ithaca, New York 14853-1301

(Received 11 March 1998; accepted for publication 12 May 1998)

We report on the performance of a Fabry–Perot resonator for far-infrared electron spin resonance (FIR-ESR) at 250 GHz designed to accommodate a thin, disk-shaped sample that must rest with its flat surface perpendicular to the incident FIR beam. This geometry minimizes dielectric losses, making it possible to obtain FIR-ESR spectra of aqueous or lossy samples with a macroscopic ordering, at canonical values of the director tilt of 0° and 90°. The resonator also utilizes an adjustable interferometer to achieve variable coupling in the FIR regime. © *1998 American Institute of Physics.* [S0034-6748(98)01608-6]

I. INTRODUCTION

High-frequency electron spin resonance (ESR) is an important technique for the study of biological systems due to its enhanced resolution to ordering and dynamics as compared to ESR at conventional frequencies.[1] For aqueous samples, the challenge is to avoid the substantial dielectric losses at 250 GHz that occur when an aqueous sample penetrates into a regime of a non-negligible far-infrared (FIR) electric field.[2] Extensive experiments with various sample geometries carried out in this laboratory have demonstrated that even a slight overlap between the sample and the resonator electric fields, on the order of submicroliter volumes, is enough to create unacceptable losses for 250 GHz ESR. Our recent development of sample holders for aqueous samples has extended our studies at 250 GHz to spin labeled biopolymers in biologically relevant environments.[3] These techniques have also made it possible to study macroscopically aligned samples such as model phospholipid membranes.[3,4] It is well known that more detailed information on the ordering and dynamics of such samples is obtained when ESR spectra are recorded as a function of director tilt angle Ψ, defined as the angle between static magnetic-field $\mathbf{B}_0$ and the macroscopic director axis.[4]

However, an aqueous sample must be geometrically matched to the lowest-order mode of the Fabry–Perot (FP) resonator in order to maximize the overlap of the sample with the $\mathbf{B}_1$ field. This achieves a higher sensitivity for ESR because it simultaneously maximizes the resonator filling factor and resonator Q by minimizing dielectric losses in the sample. When lossy solvents are present, this requires a flat, disk-shaped sample geometry that sits with the normal to its flat face parallel to the direction of propagation of the far-infrared Gaussian beam mode as it travels from the FIR source through a transmission-mode FP resonator, and on to the detector.[3] This sample geometry is shown in Fig. 1. The sample, the electric- and magnetic-field intensities, and the resonator are all cylindrically symmetric. For many cases where some macroscopic ordering is present in the sample, for example, in studies of aligned model phospholipid membranes,[4] the axis of symmetry of these samples will lie normal to the flat surface of the sample holder. Because of the design of our high-field superconducting magnet, the FIR beam propagates parallel to $\mathbf{B}_0$, so the sample holder (shown in Fig. 1 as a continuous thin box) is for the case of $\Psi=0°$. Unfortunately, this sample geometry cannot be rotated within the FP resonator to give the case of $\Psi=90°$ (shown by the dashed thin box in Fig. 1), without causing drastic dielectric losses due to its penetration into several electric-field ($\mathbf{E}_1$) maxima, as well as improper sample alignment in the $\mathbf{B}_1$ field. (Note from Fig. 1 that the $\mathbf{B}_1$ field maxima occur at the $\mathbf{E}_1$ field nodes, but have similar mode patterns.) Similarly, because the design of most superconducting, high homogeneity magnets requires that access to the area of high magnetic field be limited to a relatively long and narrow warm bore, rotating the magnet or the source/resonator/detector assembly to obtain different values of Ψ is not a realistic option.

To solve this problem, we have designed and fabricated a FP resonator that holds the disk-shaped aqueous sample at an optimum position in the resonator as before, but with the axis of symmetry of the FP resonator perpendicular to the axis of the FIR beam that travels from the source to the detector. In effect, the sample and FP resonator have been rotated by 90° in order to obtain ESR spectra with $\Psi=90°$. Together, with the original FP resonator and aqueous sample holder design,[3] this arrangement yields high-frequency ESR spectra for macroscopically aligned and lossy samples at $\Psi=0°$ and 90°. For brevity, we denote this resonator as a ''shunt'' resonator.

Since the propagating Gaussian beam from the FIR source is now orthogonal to the fundamental mode of the resonator, a different design than an iris aligned along the beam mode axis is necessary for coupling FIR radiation into the resonator. Instead, coupling is now achieved by utilizing an adjustable interferometer. This technique is a quasioptical extension of the common practice of tuning an X-band resonator by mechanically varying the effective impedance of the

[a)]Electronic mail: jhf@msc.cornell.edu

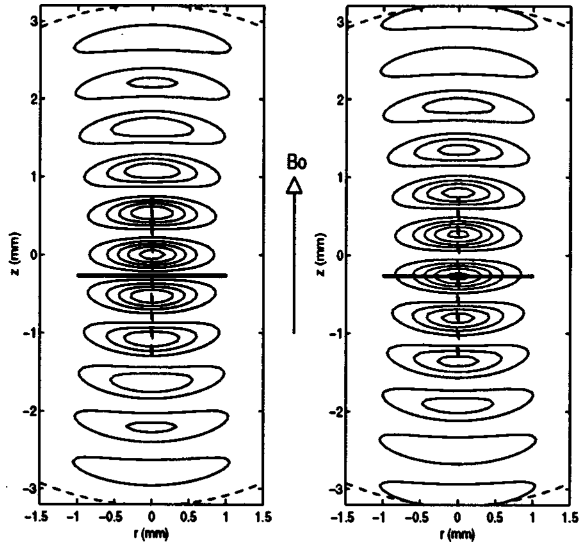

FIG. 1. A contour plot of the magnitudes of the electric field (left) and the magnetic field (right) in a Fabry–Perot resonator operating in the fundamental Gaussian beam mode. The field intensities are given at 10%, 30%, 50%, 70%, and 90% of maximum. The mirrors of the resonator are shown as dashed lines, and a disk-shaped sample is shown as a (continuous) thin box. If the normal to the thin sample lies perpendicular to the sample's flat edge (i.e., parallel to applied magnetic-field $\mathbf{B}_0$ which lies along the z axis), then this configuration represents the $\Psi=0°$ director tilt case. The $\Psi=90°$ director tilt case is shown as a dashed thin box, which will lead to unacceptable losses for samples containing water at 250 GHz.

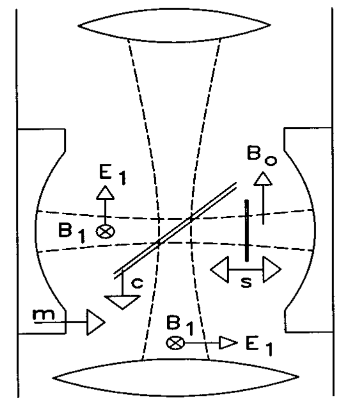

FIG. 2. A diagram of the Fabry–Perot ''shunt'' resonator in which a thin, disk-shaped and macroscopically ordered sample (s) is oriented so that the applied static magnetic-field $\mathbf{B}_0$ is 90° with respect to the sample's symmetry axis. In order to keep resonator Q and the sample filling factor high, the far-infrared Gaussian beam (the beam's radius is indicated by the dashed lines) is deflected to be perpendicular to its original axis by an adjustable interferometer (c). In order to tune the resonator, one of the spherical mirrors forming the resonator (m) can be moved. Additionally, in order to place the sample at a $\mathbf{B}_1$ field maximum, the sample itself can be mechanically moved along the resonator axis. The lenses refocus the Gaussian beam from the bottom to the top optiguide as indicated. Also, although a resonance can be found for any linearly polarized Gaussian beam mode, ESR-active polarization is indicated by $\mathbf{B}_1$ and $\mathbf{E}_1$.

resonator iris to provide optimum coupling for a given sample.[5–7] While the present FP design is fixed to provide a tilt Ψ of 90°, we also briefly indicate how the design could be modified to provide ESR spectra for any tilt angle.

II. DESIGN AND EXPERIMENTS

Figure 2 shows a scheme for the shunt resonator. The static magnetic-field direction is shown by $\mathbf{B}_0$. The dashed lines represent the beam radii of the FIR Gaussian beam modes. The lenses at the top and bottom refocus the FIR beam that travels upwards along $\mathbf{B}_0$ in the optiguide. The FIR source sits below the resonator, while the detector is above. The second set of dashed lines represents the fundamental mode of the shunt FP resonator, which is formed by the two spherical mirrors labeled as m in Fig. 2. The thin, disk-shaped sample (s) is set to one side of the FP resonator. The mirror-to-mirror distance must be adjustable in order to tune the FP resonator; additionally, as discussed before,[3] the sample position along the axis of the resonator must be independently adjustable in order to place the sample in a region of the maximum $\mathbf{B}_1$ field. This is achieved through the use of two separate cams labeled as C and I, respectively, in the exploded view of the shunt resonator assembly given in Fig. 3. Coupling between the two orthogonal FIR beams is achieved through an adjustable interferometer (c) set at a 45° angle to both modes. It is constructed from two dielectric sheets, which are separated by a small gap whose depth is adjusted by the screw labeled as F in Fig. 3.

This resonator has features intermediate between those of a transmission-mode and those of a reflection-mode resonator. A simplified model that neglects all diffractive effects of the Gaussian beam mode is sufficient to examine these features. These effects slightly lower the resonator Q and cause slight shifts in the resonant frequencies of the system. We also neglect all higher-order radial modes of the FP resonator. A description of these effects and the justification for their neglect are discussed in Ref. 3. For this simplified case, the fields in the resonator can be completely described by the seven complex field amplitudes shown in Fig. 4. They are the amplitudes of the electric field of a traveling Gaussian beam mode (for a description see Ref. 8) at the adjustable interferometer, shown as a diagonal line in Fig. 4. The arrows refer to the direction of propagation of each beam mode. The amplitudes of the modes in arm 2, into which FIR radiation from the source is reflected by the adjustable interferometer, are given by a_2^+ and a_2^-; and for arm 3, from which FIR radiation is reflected out of the resonator to the detector, we use a_3^+ and a_3^-. The FIR beam from the source has amplitude a_1^+, and the amplitude of the beam that is reflected back towards the source is given by a_1^-. The FIR beam that propagates to the detector has amplitude a_4^+.

We need to solve for a_4^+ in terms of a_1^+ and four other complex parameters which characterize the shunt resonator. They include the reflection and transmission coefficients of the adjustable interferometer: R_1 and T_1, for FIR radiation incident from either the source or from arm 2; and R_2 and T_2, for FIR radiation incident from arm 3. The two sets of coefficients might not be the same if the interferometer is not symmetrically constructed. The other two complex parameters are Γ_2 and Γ_3, which are the product of the factors for propagation down an arm (of the form $e^{2\pi i l/\lambda}$ where l is the arm length), reflection from its mirror, and then propagation back to the center point of the resonator. The magnitude of Γ is a measure of the loss of FIR amplitude due to dielectric losses in the resonator arm or to conductive losses at the

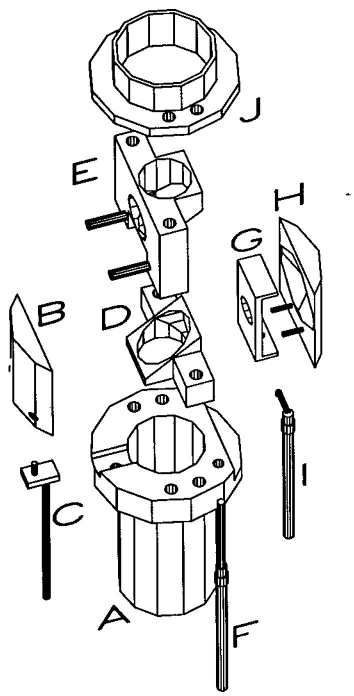

FIG. 3. An exploded view of most of the parts used to construct the shunt resonator. They are aluminum except for the modulation coil form, which was poly-(4-methylpentene-1), (TPX), and the pins, cams, and screws, which were nonmagnetic brass. (A) Platform that is also part of the optiguide to the FIR source. (B) Movable mirror and (C) the mirror's cam. (D) The bottom part and (E) the top part of the adjustable interferometer assembly, which also has pins upon which mirror B slides. The dielectric sheets that form the interferometer are glued to the angled faces of parts D and E. (F) A screw to adjust the height of part D. (G) The modulation coil form and sample holder. (H) A fixed mirror with pins on which part G slides. (I) The cam that moves part G along the resonator axis. (J) A cap for the resonator that fits into the optiguide heading towards the detector. The lenses to focus the Gaussian beam mode are held in parts A and J.

mirror. Moving the mirror in an arm will change the phase of Γ for that arm, and altering the gap in the adjustable interferometer changes the values of R_1, R_2, T_1, and T_2 (further details are given in Ref. 9).

If an ESR-active sample is placed in one of the shunt resonator arms, it modifies the value of Γ_n for that arm (where $n=2$ or 3). The effect of the ESR absorption in the shunt resonator can be represented by

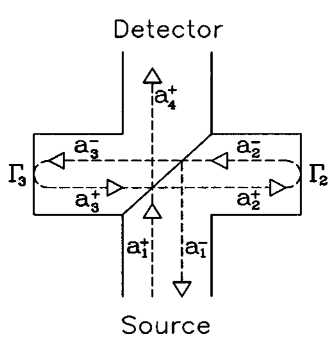

FIG. 4. The field amplitudes of the shunt FP resonator: the signal a_1^+ from the source is split by the adjustable interferometer into a_4^+ by transmission and a_2^+ by reflection; a_2^- is derived from reflection of a_2^+ from the back mirror of arm 2, and is then split into a_1^- by reflection and a_3^- by transmission; finally, a_3^+ is derived from the reflection of a_3^- from arm 3 and contributes to a_4^+ by reflection and a_2^+ by transmission.

$$\Gamma_n=(-1+c\chi)e^{4\pi il/\lambda}e^{4\pi i\sqrt{\epsilon}d/\lambda}, \tag{1}$$

where l is the length of the resonator arm, d is the sample thickness and ϵ is the sample material's complex dielectric constant, c is a constant that depends on the number of spins present and their geometric arrangement in the resonator, and χ is the complex magnetic susceptibility associated with the ESR signal. The second exponential term in Eq. (1) represents dielectric losses for the FIR beam in passing twice through the sample. Reflections from the sample surfaces are neglected. We have also assumed that $|c\chi|\ll 1$ in writing Eq. (1), i.e., the effect of the sample's ESR signal is a small perturbation on the resonator fields, which is nearly always the case. In the absence of saturation, χ is independent of $\mathbf{B}_1$, and hence, of a_n^+ and a_n^-. While more general effects such as reflection of FIR radiation from the sample and power saturation can be taken into account, for simplicity in clarifying the role of the shunt resonator we shall assume a "weak" and unsaturated ESR signal here.

To determine the strength of a magnetic-field modulation-detected ESR signal, note that a power-law detector detects the transmitted power given by $|a_4^+/a_1^+|^2$, and the strength of a magnetic-field modulation-detected ESR signal will be proportional to the first derivative of this signal with respect to $\mathbf{B}_0$, which is proportional to $\partial|a_4^+/a_1^+|^2/\partial|\Gamma_n|$ where n is the arm in which the sample sits.[10]

The set of equations for the field amplitudes are then (see Ref. 11 for further details):

$$\begin{aligned}
a_1^- &= R_1 a_2^-,\\
a_2^- &= \Gamma_2 a_2^+,\\
a_2^+ &= T_2 a_3^+ + R_1 a_1^+,\\
a_3^- &= T_1 a_2^-,\\
a_3^+ &= \Gamma_3 a_3^-,\\
a_4^+ &= R_2 a_3^+ + T_1 a_1^+.
\end{aligned} \tag{2}$$

Solving for the transmitted radiation, we have

$$\frac{a_4^+}{a_1^+}=T_1\left(1+\frac{R_1R_2\Gamma_2\Gamma_3}{1-T_1T_2\Gamma_2\Gamma_3}\right). \tag{3}$$

The tuning curve for the shunt resonator is given by $|a_4^+/a_1^+|^2$ as a function of the phase of the Γ for the arm with the adjustable mirror. It shows the same general features as observed in Fig. 5, i.e., the power incident on the detector is at a minimum when the shunt resonator is on resonance, as is the case for a reflection-mode resonator. However, the input port is physically separate from the output port, as in the case of a standard transmission-mode resonator.

The FIR radiation is not symmetrically distributed between the two arms of the shunt resonator. From the above equations, it can be shown that the maximum $\mathbf{B}_1$ field always occurs in arm 2. This suggests that the sample should be placed in arm 2 for greatest sensitivity to ESR, and also raises the question of whether the coupling into the resonator should be equal to the coupling out of the resonator, as is the

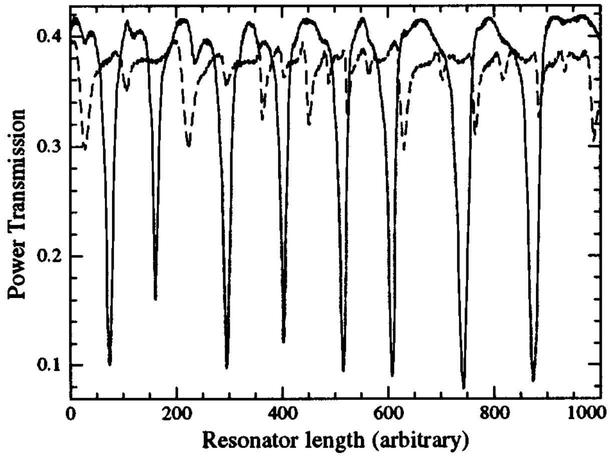

FIG. 5. Transmitted power as a function of the mirror-to-mirror separation of the shunt resonator, for two different values of d of ≈ 0.4 and ≈ 0.1 mm, corresponding to the cases of an overcoupled (dashed curve) and an optimally coupled (continuous curve) resonator, respectively. Because the mirror-to-mirror distance is adjusted manually by a cam, the spacing of the resonances appears to be irregular.

case for the transmission-mode FP resonator.[5] In order to answer these questions, examine the expressions for the ESR sensitivity: $(\partial/\partial|\Gamma_2|)|a_4^+/a_1^+|^2$ if the sample is placed in arm 2, and $(\partial/\partial|\Gamma_3|)|a_4^+/a_1^+|^2$ if the sample is in arm 3.[10] Because only the product $\Gamma_2\Gamma_3$ appears in the expression for the transmitted power, it can be seen by inspection that the ESR sensitivity of the shunt resonator is independent of which arm the sample is placed in. Even though there is more power for the spins to absorb in arm 2, partial reflection from the interferometer prevents the full signal from reaching the detector, thereby balancing out the sensitivity between the two arms.

In order to determine the coupling that maximizes ESR sensitivity, we start with the expression for the ESR sensitivity for the sample in arm 2:

$$S_2=|\Gamma_3||T_1|^2\frac{\partial}{\partial x}\left|1+\frac{|R_1R_2|e^{i(\phi+\delta)}x}{1-|T_1T_2|e^{i\phi}x}\right|^2, \tag{4}$$

where the expression is evaluated at $x=|\Gamma_2\Gamma_3|$. As $|\Gamma_2\Gamma_3| \to 1$, FIR losses in the shunt resonator decrease to zero and the resonator Q depends only on the coupling. The phase of the term $T_1T_2\Gamma_2\Gamma_3$ is given by ϕ, and the phase difference between R_1R_2 and T_1T_2 is given by δ. If we assume that the interferometer is lossless, then we can set $|R_1|=\sin\alpha$, $|T_1| =\cos\alpha$, $|R_2|=\sin\beta$ and $|T_2|=\cos\beta$. The coupling that maximizes ESR sensitivity will occur at the global extremum of $S_2(\alpha,\beta,\delta,\phi)$. It can be shown that there are several extrema of S_2 as a function of δ and ϕ, but the global maximum occurs for $\delta=\phi=0$. Since ϕ is the total phase change of a FIR beam as it makes one round trip in the shunt resonator, the condition $\phi=0$ simply states that the shunt resonator should be tuned on resonance for maximum sensitivity. We then have that

$$S_2=2|\Gamma_3|\cos^2\alpha\sin\alpha\sin\beta \times\frac{1+|\Gamma_2\Gamma_3|(\sin\alpha\sin\beta-\cos\alpha\cos\beta)}{(1-|\Gamma_2\Gamma_3|\cos\alpha\cos\beta)^3}, \tag{5}$$

for which it can be found that global maxima occur for various values of $|\Gamma_2\Gamma_3|\leqslant 1$ near $\alpha=\beta$. For example, when $|\Gamma_2\Gamma_3|\approx 0.9$, the maximum sensitivity occurs for $\alpha\approx 0.3$, with α decreasing as the resonator Q increases. Thus, the adjustable interferometer should be constructed symmetrically, using two dielectric sheets of equal thickness.

In determining the needed radii of the lenses and the mirrors, the most important consideration in the design was the space constraint: the resonator had to fit within the warm bore of our superconducting magnet, so its overall diameter was limited to 45.5 mm. The other main requirements are that the Gaussian beam mode incident from the bottom optiguide with a beam waist radius of $\omega_0=4.5$ mm must match the Gaussian beam mode focused into the top optiguide with $\omega_0=6.7$ mm. The beam waist radius should be centered on the adjustable interferometer to minimize walk-off losses.[12] The choice of a beam waist radius is a compromise between a small enough radius to fit the beam within the aperture for the interferometer, and a large enough radius so that losses of radiation out the side of the open resonator due to beam divergence do not significantly degrade the resonator Q. Our size constraints limited both the interferometer aperture and the mirror extent. Our final design has a 16 mm diam aperture for the interferometer (the circular bore holes in parts D and E of Fig. 3), and a mirror radial extent of 16.3 mm. At the interferometer, $\omega_0=2.31$ mm, while at each mirror the beam radius grows to ≈ 4.1 mm. The mirror radii of curvature are 30.0 mm, and the mirror-to-mirror distance can be varied from 40.4 to 33.3 mm. As the cam (part C of Fig. 3) is turned, the FP resonator tunes through >10 resonances.

Any semireflective, nonlossy surface, such as a wire mesh grid or a thin sheet of dielectric, can be used for the interferometer. We used Mylar (polyethylene terephthalate) because it is available in high-quality sheets of various thickness, from 0.01 to 0.50 mm, and is stiff enough to remain flat across a 16 mm span. The index of refraction for Mylar is $n=1.8$ with a loss tangent of around 0.01 at 250 GHz (see Ref. 13 for a list of the complex dielectric constants of various materials used in the FIR regime). Although Mylar has a larger loss tangent than many other dielectrics,[13] this does not represent a drawback, because the resonator Q is limited by dielectric losses in the aqueous sample. Sheets of 0.25 mm thick Mylar were glued to their frames (parts D and E of Fig. 3) using a silicone adhesive. Two 0.05 mm thick sheets were tried, but they resulted in an undercoupled resonator that could not be adjusted to a critically coupled state. Shown in Fig. 5 are two power transmission curves for the empty shunt resonator, in which the influence on the resonator Q of varying the gap between the two Mylar sheets can be observed.

In order to understand why the 0.25 mm thick Mylar sheets worked well, we examine the performance of the adjustable interferometer as a function of dielectric sheet thicknesses and materials. The method of solution is similar to that of Ref. 9, so we only give the results here. If a single dielectric sheet is used as the beam splitter, then we can use an Airy function for the reflection of a plane wave off a dielectric sheet:

$$R(\text{sheet})=r_e+\frac{r_i t_e t_i e^{2i\theta}}{1-(r_i e^{i\theta})^2},\quad T(\text{sheet})=\frac{t_e t_i e^{i\theta}}{1-(r_i e^{i\theta})^2},\tag{6}$$

where r_e, r_i, t_e, and t_i are the reflectivities and transmissivities for a plane wave of a fixed polarization from outside and inside the dielectric, respectively, and θ is the phase due to propagation through the dielectric sheet.[14] For Mylar, the shunt resonator is undercoupled for sheet thicknesses of 0.31 mm and for the case where no dielectric is present (i.e., at a sheet thickness of 0 mm, no FIR radiation is shunted into the Fabry–Perot resonator). At 0.16 and 0.47 mm thickness, a very broad tuning dip indicates an overcoupled resonator. At intermediate values of 0.08, 0.23, and 0.39 mm, the empty resonator is optimally coupled. For variable tuning, we can use the above expressions for the reflection from a single dielectric sheet into a second Airy function that models the reflectivity of an interferometer consisting of two dielectric sheets separated by a gap of d. Using 0.25 mm thick Mylar sheets gives the adjustable interferometer a wide range in reflectivities to allow for a full range of coupling upon varying d. Thinner sheets undercouple the resonator for any value of d, while thicker sheets would lower the resonator Q unnecessarily.

Note that the resonator supports both linearly polarized modes. The Q of the resonator changes as the polarization vector is rotated, due to the dependence of the reflectivities of the dielectric sheets upon the $\mathbf{E}_1$ field polarization.[14] However, only one polarization is maximally ESR active: that in which the $\mathbf{B}_1$ field remains perpendicular to $\mathbf{B}_0$ at the sample, as shown in Fig. 2. Because of these facts, this resonator has a partial ''bimodal'' property to it. In fact, if the angle between the Fabry–Perot resonator axis and that of the optiguide axis could be altered to match the Brewster angle of a dielectric sheet, then the resonator could act as an induction-mode resonator, although we mention that it would probably be better to use wire grid polarizers if such a mode of operation was desired.[5]

Reasonable optimal alignment in the FIR is ensured by keeping tolerances at a level that can be achieved using standard machine shop practices ($\pm$0.001 in. for dimensions, and $\pm$5° for angles between surfaces). Most of the components are aluminum or brass, so that thermal stresses would not cause moving parts to lock up. Temperature control is achieved by flowing dry nitrogen gas through the entire resonator space, with input and output ports on either side of the TPX coil form. We have stabilized the temperature in the resonator from -10 to $+70$ °C, although at higher temperatures the thin Mylar sheets curl up. The TPX modulation coil form (part G in Fig. 3) had 100 turns of 30 awg wire wrapped in bands immediately above and below the sample, which is held on a circular ledge. The TPX frame can be moved by its cam $\approx$1 mm in order to set the sample at a point of maximum $\mathbf{B}_1$ field. In general, it is best to keep the sample as close to the adjustable interferometer as constraints allow, since the sample will then be closer to the beam waist where the field surfaces have a greater radius of curvature.[3] Because of the limited diameter of the superconducting magnet's warm bore, the amplitude of the modulation field is somewhat lower than we usually use. It is expected that the sensitivity of this device could be improved for a larger warm bore, a higher modulation field, or the implementation of a different modulation scheme.[15]

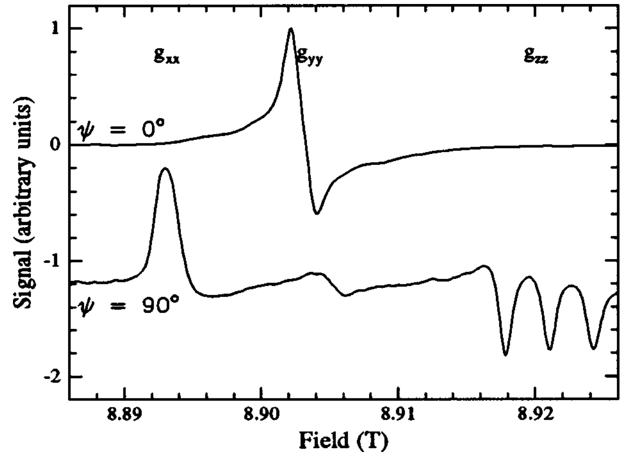

FIG. 6. 250 GHz ESR spectra of a macroscopically aligned model phospholipid membrane at two different values of the director tilt. The difference in the two line shapes is indicative of the extra information for ordering and dynamics that is available when ESR spectra at both Ψ=0° and 90° are obtained.

We demonstrate the use of this resonator with the following example.[16] Shown in Fig. 6 are 250 GHz ESR spectra of a macroscopically aligned model phospholipid membrane (80 mol % 1,2-dimyristoyl-*sn*−glycero-3-phosphatidylcholine to 20 mol % 1,2-dimyristoyl-*sn*−glycero-3-phosphatidyl-*L*-serine). The alignment of the membrane is such that the normal to the surface of the membrane $\hat{n}$ is parallel to the cylindrical axis of the disk-shaped sample holder. The membrane is fully hydrated and these spectra were obtained at 10 °C, so the sample must be treated as very lossy to FIR radiation. The nitroxide spin label is a cholesterol analog (CSL, 3-doxyl-5α-cholestane). CSL is present at a 3 mol % concentration, which for the $\approx$1 mg sample translates into 3×10^{16} spins in a sample volume of <1 μl. CSL aligns in the membrane such that the nitroxide N–O bond (the $\hat{x}$ axis of the molecule) and the axis along the nitrogen p orbital (the $\hat{z}$ axis) both lie perpendicular to $\hat{n}$. Due to the anisotropy of the g tensor, the ESR resonant field occurs at different values when B_0 is parallel to $\hat{x}$, $\hat{y}$, or $\hat{z}$ of the nitroxide, as is labeled in Fig. 6. The top spectrum was recorded in our standard Fabry–Perot transmission-mode resonator, for which $\mathbf{B}_0$ is parallel to $\hat{n}$, and the single sharp peak demonstrates that CSL orients with its $\hat{y}$ axis parallel to $\hat{n}$. When this same sample is placed in the shunt resonator, $\mathbf{B}_0$ is now perpendicular to $\hat{n}$, and as a result the ESR spectrum ''sees'' CSL oriented with its $\hat{x}$ axis or its $\hat{z}$ axis parallel to $\mathbf{B}_0$ with equal probability. It is precisely this kind of resolution to ordering provided by FIR-ESR that drives the need for the shunt resonator.

Finally, we briefly note that more extensive information on ordering and dynamics would be obtained if ESR spectra with any tilt angle were available. There are at least two ways to accomplish this. One could modify the current design to allow the axis of the Fabry–Perot resonator to rotate within the warm bore of the superconducting magnet. For angles near 0°, the mirrors begin to block the Gaussian beam from the source, but angles from ≈30° to 90° could be obtained. However, we advocate a second approach in which the axis of the FP resonator is rotated at any angle with respect to $\mathbf{B}_0$, and the axis of the FP resonator is horizontally offset from the axis of the optiguide in order to prevent any part of the resonator from ''shadowing'' the optiguide beam. Coupling is through a pair of flat 90° mirrors, one of which rotates fixed with the FP resonator. This approach would require a warm bore radius of at least 80 mm.

III. DISCUSSION

In summary, we have designed, constructed, and tested a shunt resonator for high-frequency ESR that utilizes variable coupling through dielectric sheets. We have demonstrated its usefulness on a macroscopically aligned and fully hydrated model phospholipid membrane. We have also discussed how the sensitivity and the design could be improved, and how it might be extended to the case of different tilt angles.

ACKNOWLEDGMENTS

The authors wish to acknowledge helpful discussions with Dr. Keith Earle. This work was supported by NIH Grant Nos. RR 07216 and GM 25862. One of the authors (J.P.B.) was supported by National Research Service Award No. GM 17174.

[1] D. E. Budil, K. A. Earle, and J. H. Freed, J. Phys. Chem. **97**, 1294 (1993).
[2] Measurements of the complex dielectric constant of water from 1 GHz into the far infrared can be found in J. B. Hasted, *Aqueous Dielectrics* (Chapman and Hall, London, 1973), Chap. 2; J. Barthel, K. Bachhuber, R. Buchner, and H. Hetzenauer, Chem. Phys. Lett. **165**, 369 (1990); J. B. Hasted, S. K. Husain, F. A. M. Frescura, and J. R. Birch, Infrared Phys. **1**, 11 (1987); M. N. Afsar and J. B. Hasted, J. Opt. Soc. Am. **67**, 902 (1977).
[3] J. P. Barnes and J. H. Freed, Rev. Sci. Instrum. **68**, 2838 (1997).
[4] M. Ge, D. E. Budil, and J. H. Freed, Biophys. J. **67**, 2326 (1994).
[5] K. A. Earle, D. E. Budil, and J. H. Freed, in *Advances in Magnetic and Optical Resonance*, edited by W. S. Warren (Academic, San Diego, 1996), Vol. 19.
[6] W. B. Lynch, K. A. Earle, and J. H. Freed, Rev. Sci. Instrum. **59**, 1345 (1988).
[7] K. A. Earle, D. S. Tipikin, and J. H. Freed, Rev. Sci. Instrum. **67**, 2502 (1996).
[8] J. Lesurf, *Millimeter Wave Optics, Devices and Systems* (Adam Hilger, Bristol, 1990), Chap. 1.
[9] A. C. de C. Lima and E. A. Parker, IEE Proceedings-Microwaves, Antennas, and Propagation **143**, 157 (1996).
[10] G. Feher, Bell Syst. Tech. J. **36**, 449 (1957); see also, C. P. Poole, Jr., *Electron Spin Resonance: A Comprehensive Treatise on Experimental Techniques* (Interscience, New York, 1967), Chap. 14.
[11] R. E. Collins, *Foundations for Microwave Engineering*, 2nd ed. (McGraw-Hill, New York, 1992), Chaps. 3 and 4.
[12] J. A. Arnaud, A. A. M. Saleh, and J. T. Ruscio, IEEE Trans. Microwave Theory Tech. **22**, 486 (1974).
[13] J. W. Lamb, Int. J. Infrared Millim. Waves **17**, 1997 (1996).
[14] J. D. Jackson, *Classical Electrodynamics*, 2nd ed. (Wiley, New York, 1962), Eqs. 7.39 and 7.41.
[15] P. B. Sczaniecki, J. S. Hyde, and W. Froncisz, J. Chem. Phys. **94**, 5907 (1991); H. S. Mchaourab and J. S. Hyde, *ibid.* **98**, 1786 (1993).
[16] J. P. Barnes and J. H. Freed, Biophys. J. (in press).